Selective laser melting of partially amorphous regolith analog for ISRU lunar applications

Julien Granier, Thierry Cutard, Patrick Pinet, Yannick Le Maoult, Serge D. Chevrel, Thierry Sentenac, Jean-Jacques Favier

Selective laser melting of partially amorphous regolith analog for ISRU lunar applications

Julien Granier [a,b,*], Thierry Cutard [a], Patrick Pinet [b], Yannick Le Maoult [a], Serge Chevrel [b], Thierry Sentenac [a], Jean-Jacques Favier [c,1]

[a] Institut Clément Ader (ICA), Université de Toulouse, CNRS, IMT Mines Albi, INSA, ISAE-SUPAERO, UPS, Campus Jarlard, F-81013, France
[b] Institut de Recherche en Astrophysique et Planétologie (IRAP), CNRS, CNES, Observatoire Midi-Pyrénées, Université de Toulouse, France
[c] IMT Mines Albi, Campus Jarlard, F-81013, France

Keywords:
Lunar regolith
SLM
Annealing
Compressive strength
Ceramics
Glass

As the idea of crewed outposts on the Moon gains momentum, In-Situ Resource Utilization (ISRU) technologies tend to become imperative to fulfill astronauts' needs. This article explores a way to use the lunar regolith as a source material for the additive manufacturing of complex objects, based on the selective laser melting (SLM) technique. A lunar regolith analog, Basalt of Pic d'Ysson (BPY), is used as a starting point for this study, to investigate the now demonstrated impact of amorphous analog content in the powder bed, substrate type, and post-SLM annealing treatments on the mechanical properties of 3D-printed objects. Improvements to the manufacturing and sample extraction stages are proposed to systematically reproduce the high compressive strength values obtained, thus contributing to the robustness and reliability of the process.

1. Introduction

Over the last decade, the Moon has again become the focus of attention, and the priority of many space programs, not only from the USA [1] but from China [2], Russia, India [3], Japan [4] and Europe [5] as well. Establishing a permanent crewed outpost on the lunar surface is a key milestone in developing scientific research capabilities and exploitation facilities. Those outposts will have to ensure a large panel of vital functions for the astronauts, such as radiation protection [6], food, water and oxygen supplies, and structural tools for astronauts' daily operations, requiring overwhelming quantities of raw materials and energy. Confronted with the difficulty of sending large quantities of material from Earth to the Moon, the In-Situ Utilization of Resources (ISRU) such as solar light and materials from the lunar regolith, has been the subject of significant technological development in recent years [7]. Additive manufacturing, because of its inherent absence of waste material and its flexibility, is one of the most interesting fields for manufacturing objects [8], divided into two main categories. Indirect methods like ink extrusion [9], cement contour crafting [10], or digital light processing [11] are defined by the use of binding products to shape the manufactured structures. They can reach higher production rates [12], provide elastic properties to the regolith [9], or reach particularly high compressive strength as 428 MPa [11]. However, in a lunar outpost context, these properties come with the sacrifice of devoting a significant portion of the payload to binders and equipment for the heating post-treatments, often needed for debinding and sintering steps.

In contrast, direct additive manufacturing techniques based on the direct sintering or melting of the regolith like microwave processing [13] or powder bed fusion [14–18] have the advantage of not requiring any organic binder and do not necessarily need any post-treatment. However, because of the high thermomechanical stresses induced into the manufactured objects and without an appropriate post heat treatment, they also tend to lead to weaker mechanical properties. Direct sintering or melting of the lunar regolith materials implies a good understanding of their behavior when being subjected to an important energy source. The use of simulants [19], especially chosen for their chemical composition, grain size distribution and morphology close to the lunar soil, allows the measurement of physical properties like reflectance [20,21], thermal conductivity [22,23], phase transformations over temperature and sintering behavior [24,25]. A few laboratories already started conducting selective laser melting experiments on simulants, giving a first important piece of information about

* Corresponding author. IMT Mines Albi - allée des sciences, 81000, Albi, France.
E-mail address: julien.granier@mines-albi.fr (J. Granier).
[1] In memoriam

process parameters like energy density [14,26] and the effect of environmental parameters such as vacuum and low gravity [15,27]. The effect of regolith's variable composition remains still unclear, in particular due to its amorphous parts. Glassy components are naturally present in significant quantities, particularly in mature regolith and for small granulometric sizes, as a result of meteorite impacts and lunar volcanic activity, going up to 90 % in extreme cases [28,29]. Simulants like JSC-1A/JSC-2A have an initial amount of volcanic glass which has an identified effect on a few thermal properties [24,30] without suggesting or pointing out any particular impact on the additive manufacturing process.

This study aims to use a self-prepared and tunable regolith analog called BPY (i.e., Basalt of Pic d'Ysson) in a Selective Laser Melting process, to determine the effect of different parameters related to the nature of the powder itself (amorphous or/and crystalline structure), or operating conditions (type of substrate, annealing post-treatment) on the compression mechanical behavior of manufactured samples. Relationships between the mechanical properties, the microstructure and the operating conditions of those samples are also investigated, in order to assess at the same time the influence of the natural range of composition of the lunar regolith and the processing strategy to manufacture objects with optimized microstructures and mechanical properties.

2. Materials and method

2.1. Basalt of Pic d'Ysson (BPY) as a lunar analog

The Basalt of Pic d'Ysson, used as a lunar regolith analog, is an unweathered basaltic lava flow from the Massif Central in France, initially used for optical properties modeling for orbital remote sensing applications [20]. The preparation of the original BPY analog is described by the black path in Fig. 1.

Basalt blocks are selected to be at least 10 cm in thickness so that most of the material is unaltered. Unweathered basalt can be recognized by a dark grey matrix and the presence of pronounced green olivine phenocrysts. All the blocks are then cleaned with a high-pressure, high-temperature water jet to remove any possible traces of organic matter, dried in an oven at 80 C for 12h, crushed into a first gravel then milled twice (disk crusher then vibrating cup crusher). The resulting powder has a particle size distribution within the limits of the samples returned by the Apollo missions [31], with a median size of 80 µm, as shown in Fig. 2.

XRD (X-Ray Diffraction) analyses have been conducted on both native and amorphous BPY, with a Malvern PANalytical Empyrean Series 3 X-ray diffractometer in Bragg-brentano geometry using a copper anode with a scan step size of 0.033° and a time per step of 200s, XRD diagrams are shown in Fig. 3. The crystalline phases contained in the native BPY are plagioclases (anorthite, nepheline), olivines (forsterite), pyroxenes (diopside, augite) and iron-rich oxides (magnesioferrite, magnetite, ilmenite).

The crystalline phases identified by XRD phases match the global composition of an alkali basalt when completed with chemical

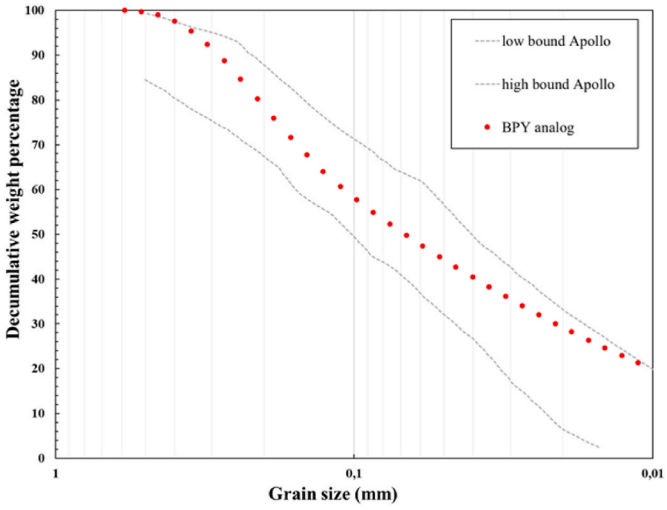

Fig. 2. Particle size distribution of the BPY analog determined by laser diffraction granulometry compared to regolith samples from Apollo missions.

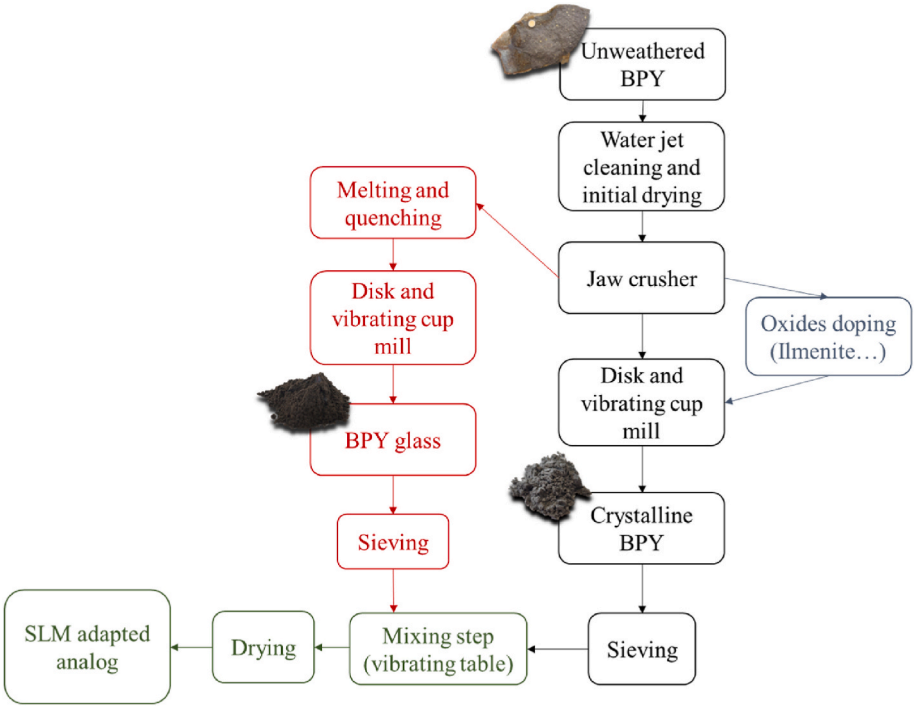

Fig. 1. Main steps of BPY analog preparation.

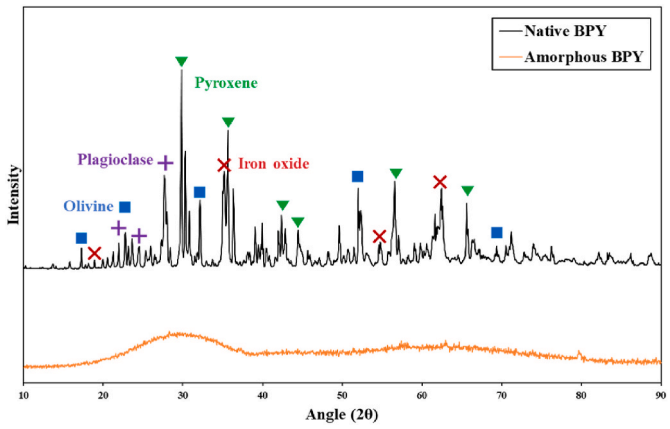

Fig. 3. XRD diagrams of native BPY powder and of its amorphous counterpart (powder too), with main identified peaks.

composition, as shown in Table 1 and obtained with the help of ICP-MS experiments [32]: BPY powder has been analyzed by CRPG rock analysis facilities (Nancy, France), crushed under 80 µm. Three measurements have been conducted on 3 different samples of 200 mg. The presented chemical composition in Table 1 is an average of those 9 values.

Compared to the lunar samples and most common simulants (Fig. 4), BPY can be considered close to a low Ti mare basalt analog (i.e., 1 to 4.5 wt% TiO_2 [33]). When used for additive manufacturing, it is then dried again in an oven at 80 C for several hours and sieved between 40 µm and 200 µm to ensure good flowability during the powder spreading, as described in 2.2.

This process described to obtain the generic BPY analog can be coupled with oxide and glass doping. The glassy phase used in this study is created directly from the initial BPY melted at 1400°C in a platinum crucible then quenched by pouring the liquid glass on a water-cooled plate. The obtained amorphous material then follows the same preparation as the original BPY analog, resulting in particles with the same size distribution and shapes as shown in Fig. 5. XRD analysis from Fig. 3 confirmed that no crystalline phases remained at the end of the melting-quenching process. Accordingly, the controlled mixing of both the crystalline and amorphous phases can be fully addressed in a quantified way in the experiments. This mixing step is done by placing the two powders in a same cup attached to a vibrating table for an hour.

From the perspective of additive manufacturing, thermal properties characterization during a first thermal cycle has been conducted, in particular a Differential Scanning Calorimetry (DSC) at high temperature completed with a Mettler Toledo TGA/DSC3+ HT device. Results are given in Fig. 6. The experiment consisted of a two-crucible system: one sacrificial alumina crucible containing the sample, and one covering sapphire crucible to block any radiation coming from the sample. The applied thermal cycle is a progressive heating from 100°C to 1500°C at 10°C/min, then cooling down at the same rate until 100 C, all under argon atmosphere. This cycle was first applied to the two-crucible system alone, and the resulting blank signal was subtracted from the analog analysis trials. Both for the crystalline and amorphous analogs, 70 mg of material have been used. Despite all the different phases initially present in BPY, only one melting area has been detected, with a wide peak centered at 1150°C. In the case of the amorphous BPY, two new phenomena appear: a glass transition temperature close to 670°C, which can differ between simulants depending significantly on sodium concentration [39], and an annealing area with two peaks (at 788°C and 830°C), due to the cold crystallization of the amorphous basalt into a phase encompassing two closely related crystal structures, called diopsidic augite [40].

2.2. Additive manufacturing

Direct additive manufacturing experiments have been conducted with an SLM125HL machine from SLM Solutions, with the working area described in Fig. 7. The BPY analog powder comes from a feedstock tank placed on top of the machine, it enters in cavities craved in a turning barrel which controls the quantity of powder distributed, then it slides along a distribution slope into the recoater, and it is finally equally spread along the building platform by means of a rubber blade. A Nd-YAG laser (λ = 1064 nm) can then be focused on the powder plane surface, drawing the shape of the object by the formation of a moving melting pool that quickly solidifies. The building platform is then lowered from a precise given value to receive a new powder layer. An inert atmosphere is created with a unidirectional argon inlet. Due to the chemical nature of regolith analogs and simulants, the building platform requires an adaptation by putting an intermediate ceramic substrate as described in the next paragraph. A thermal paste is applied to the bottom of the intermediate substrate to ensure good heat conduction with the metallic plate of the machine, during the pre-heating stage at 200°C. This preheating step is essential to limit extreme thermal gradients between the melting pool and the rest of the powder, which could damage and/or deform the printed objects. The final state of the material highly depends on the Volumetric Energy Density (VED, J/mm^3) provided by the laser, and is described in this work by the simplified following equation:

$$VED = \frac{P}{v \cdot e \cdot h}$$

With P the laser power (W), v the laser scanning speed (mm/s), e the powder layer thickness (mm), and h the laser hatching distance (i.e., the distance between two consecutive and parallel laser scanning vectors, mm). In the case of the BPY analog, an optimal range of volumetric energy density has been found with the parameters described in Table 2, leading to a volumetric energy density between 10 kJ and 16 kJ/cm^3. These parameters are for now the best-found compromise to limit porosities coming from the material vaporization and lack of fusion effects at the same time, as illustrated in Ref. [41].

In this study, the effect of the following parameters on the microstructure and mechanical properties of 3D printed samples have been explored.

- The choice of the substrate. Three different kinds of ceramic materials have been selected, and used as 1 cm thick platforms, with a square surface of 5 × 5cm^2. Blocks of vitreous silica and BPY have been directly cut from preexisting bulks with a diamond blade saw. On top of those two different possibilities, a 1 mm thick layer of BPY powder sintered at 1100°C for 5h on top of a thin vitreous silica layer has also been used.
- The powder amorphous to crystalline ratio, with a variation between 0 %, 50 wt%, and 100 % in the glass content.
- The effect of a thermal post-treatment: some samples from the same 3D printing session have been selected for an annealing program consisting of heating at 10°C/min until 900°C, of 1h isothermal dwell at 900 C, triggering the cold crystallization described in section

Table 1
Average BPY chemical composition determined with mass spectroscopy (L.O.I. = Loss Of Ignition).

Oxide	SiO_2	Al_2O_3	Fe_2O_3	MnO	MgO	CaO	Na_2O	K_2O	TiO_2	P_2O_5	L.O.I.
wt. %	42,1	12,6	12,3	0,2	12,1	10,5	3,2	1,3	2,7	0,8	1,1

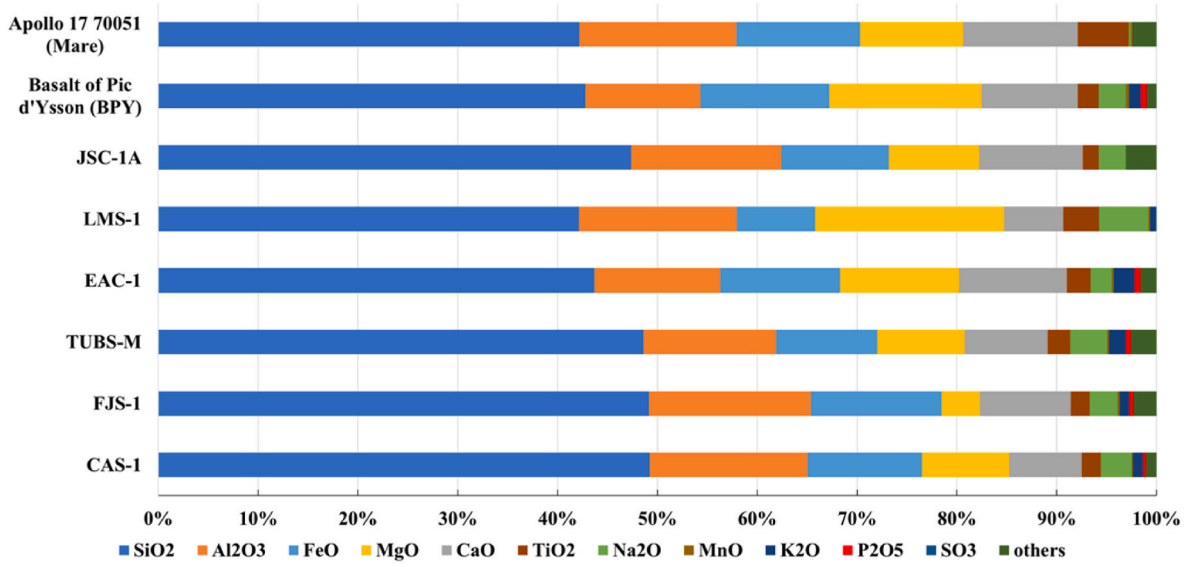

Fig. 4. Chemical composition (wt%) of an Apollo Mare sample compared to the BPY analog and several mare simulants [28,34–38].

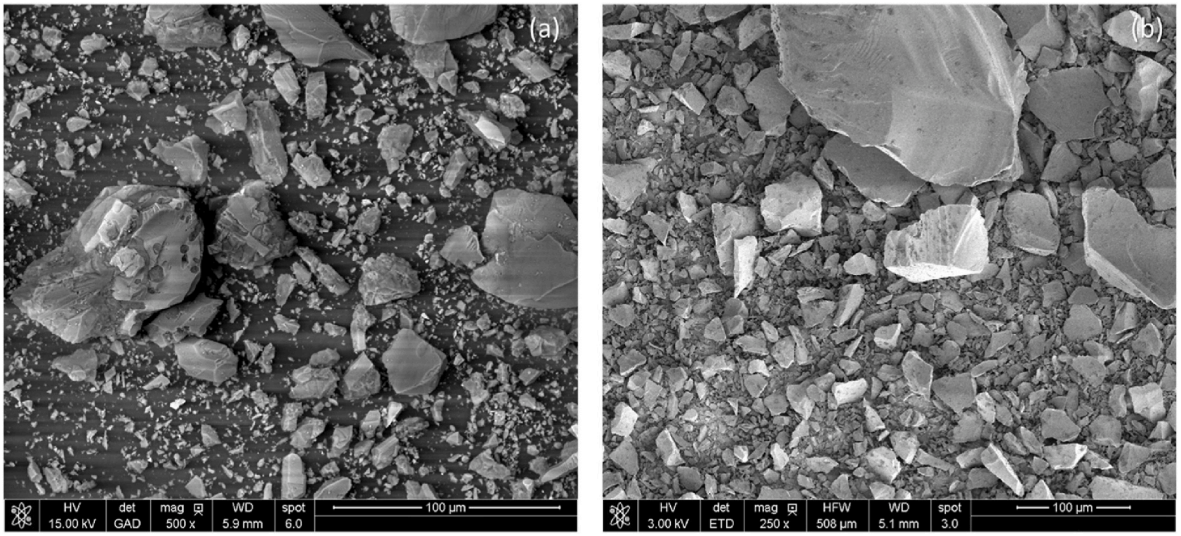

Fig. 5. Comparison of SEM images of (a) the BPY crystalline analog and (b) the BPY glass analog.

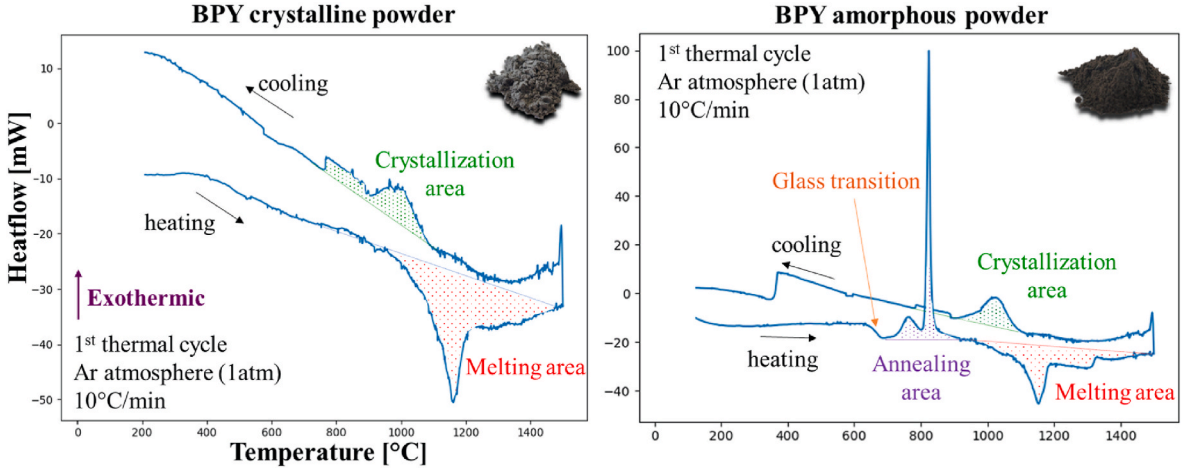

Fig. 6. Differential Scanning Calorimetry of (a) initial BPY basaltic powder and (b) BPY amorphous powder.

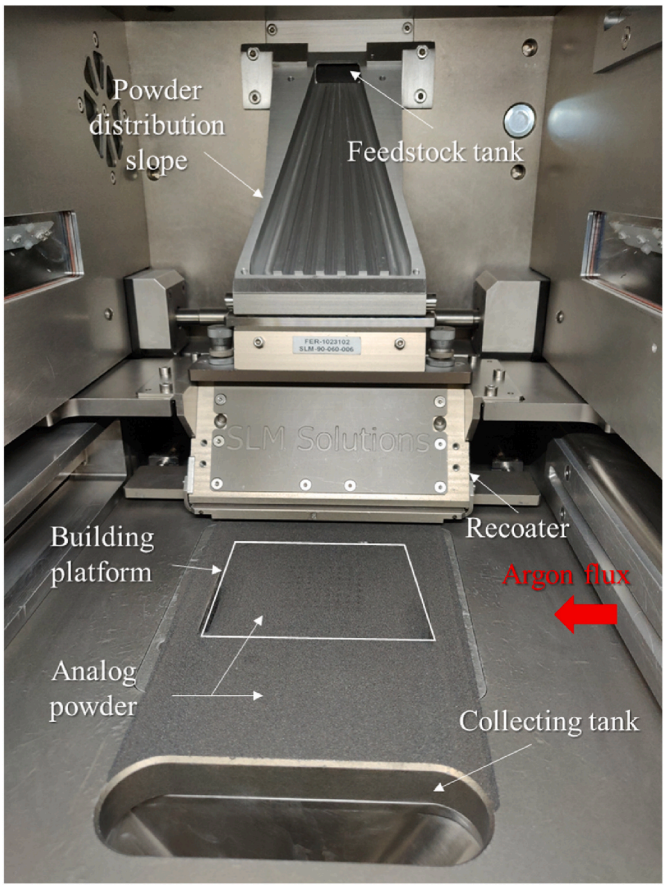

Fig. 7. View of the working area of the SLM125HL machine.

Table 2
Summary of the different sets and values considered for SLM tests.

Processing parameters	Parameters range
Substrate	vitreous silica, bulk BPY, sintered BPY powder
Powder	100 % crystalline BPY powder, mix of 50 wt% amorphous and 50 wt% crystalline BPY powders, 100 % amorphous powder
laser power (P)	34–56W
wavelength	1.06 µm
laser spot size	60 µm
hatching distance (H)	55 µm
scanning speed (V)	150–250 mm/s
First layer thickness (E)	0,5–0,6 mm
Other layers thickness (E)	0,2–0,3 µm

2. The samples and their substrate are then slowly cooled down to room temperature at 10°C/min.

The nomenclature used in the following results section to describe a configuration as a function of those parameters is described in Table 3.

When the 3D printing step is finished, the manufactured samples require a separation procedure as follows: paraffin is melted at 70°C and poured on the substrate, trapping the samples as they cool down and solidify. Then, a diamond blade is used to saw the substrate as close as possible to the base of the BPY samples. The two sides of the paraffin blocs can then be polished with SiC paper until both surfaces are smooth, parallel, and make apparent the top and bottom of the BPY samples. Samples are then extracted from the paraffin in an oven with a temperature set at 70°C.

Table 3
Adopted nomenclature to reference the manufacturing conditions for the various samples in the study.

	Type of BPY analog powder	/	Type of substrate	/	Annealing post-treatment
Notation	**C**		**S**		*Not annealed*
signification	*100 % **C**rystalline*		*Silica*		
	CA		**B** *bulk Basalt*		**an**
	*50 wt% **C**rystalline/50 wt % **A**morphous*				*Annealed*
	A		**BS**		
	100 % amorphous		*Sintered **B**PY powder layer on **S**ilica*		
Examples	C/S: BPY 100 % crystalline/Silica substrate/Not annealed C/B/an: BPY 100 % crystalline/Bulk basalt substrate/Annealed CA/S/an: BPY 50 wt% crystalline - 50 wt% amorphous/Silica substrate/Annealed				

2.3. Mechanical tests

Compressive tests have been conducted on a 30 kN Instron 5967 electromechanical machine, with the set-up described in Fig. 8. Loading is applied to the samples via a displacement of the upper steel support (linked to the mobile crosshead) at a constant rate of 0,025 mm/s. Cylindrical samples are compressed along their axis and perpendicularly to the 3D printed layers. Because of the separation procedure, the bottom and the top parts of the cylinders are indistinguishable, as well as their initial position on the additive manufacturing substrate. Evolutions of the load and the crosshead displacement values have been recorded. Load values have been converted into stress ones by measuring the initial diameter of each sample and calculating the transversal section value. To obtain sample strain values, the bench stiffness has been determined by making a compression test on a 2024T3 aluminum alloy sample having the same length as regolith analog samples. Considering the Young's modulus of 77 GPa for this aluminum alloy, the bench stiffness has been evaluated at 14826 kN/mm, thus allowing a displacement correction and calculating the sample strain.

Vickers micro-hardness has been determined using a Buehler OmniMet MHT1600-4980T, applying a load of 100gf for 10s on the samples.

2.4. Porosity calculations

The density of the native BPY powder has been estimated at 3066 g/cm^3 with a Micromeritics ACCUPYC II 1340 gas pycnometer, under a

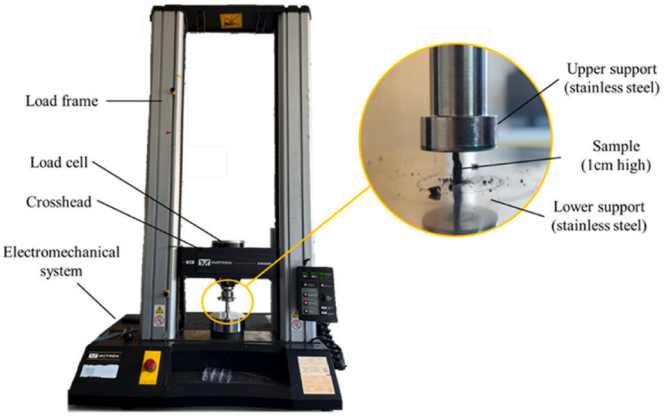

Fig. 8. Description of the compression bench.

helium atmosphere. This estimate is the basis for the porosity calculations in the results section. Assuming that the density of the manufactured objects leaving the process is the same as that of the original basalt, we can then determine the relative density of the samples (including closed porosities), relate the samples relative density to the density of the native basalt, and determine approximate porosity values. These values are therefore based on a strong assumption, but which makes possible the comparison of porosity levels quantitatively between different samples. The relative density of the samples is determined with a lab scale Sartorius LA3200DC equipped with a Sartorius YDK 01 density determination kit, using the Archimedes' principle comparing sample weight measured in both air and water, as indicated in the following equation:

$$\rho_{sample} = \frac{m_{air}}{m_{\text{air}} - m_{water}} \cdot \rho_{water}$$

with ρ_{sample} the density of the sample, m_{air} the mass of the sample in air, m_{water} the mass of the sample in water, and ρ_{water} the density of water.

3. Results

3.1. Early printing problematics and preliminary sample shape and substrate material selection

Before proceeding to mechanical tests, a first step was to make additive manufacturing viable and select an optimal object shape that could be easily reproduced. On samples with large form factors, a consistent phenomenon of edge lift, related with the wrapping effect documented in the literature ([42]), could be observed, as shown on Fig. 9 on parallelepipedal samples (26 mm long, 6 mm tall and 2,5 mm wide). This lift can be attributed to several factors with undetermined magnitude: extreme thermal gradients in the material, surface tension in the melting pool, and difference in thermal expansion coefficients between the substrate and the SLMed material. Two axes have been considered to mitigate this phenomenon: while preheating the substrate at 200°C was a way to limit extreme thermal gradients, changing its nature was intended to limit the effect of the thermal expansion coefficient difference. Considering substrates of vitreous silica or of bulk BPY had no observable effect on the lifting phenomena. In contrast, using a sintered layer of BPY powder on silica as a substrate greatly improved the parallelepipeds quality, with less than a half of the samples exhibiting a lift. This shows that while the chemical nature of the substrate does not matter significantly, other physical properties, as surface roughness have an important role in the process. The detailed reasons for this gain in quality are still to be investigated. A first hypothesis could be that the coarse layer of sintered powder represents a good intermediate medium, closer in porosity and aspect to the free BPY analog powder bed. This gradual transition between powder and solid bulk could create a tougher interface at the sample base, reducing in the same way possible defects in that area. Another hypothesis is that the thermal expansion of the substrate is opposed to the retractation movement of the powder being melted, creating a mechanical stress once again limited by the gradual interface provided by the sintered powder layer.

It is important to note that when considering objects with small contact surfaces with the substrate, lifting effect is not observed. In consequence, the next sections commenting mechanical properties will be focused on produced cylinders with a height of 10 mm and a diameter of 3 mm, which are the easiest items to reproduce accurately in terms of length, diameter and parallelism between faces, an important aspect being considered for compressive tests.

The impact of the substrate type on the efficiency of additive manufacturing is also reflected in the mechanical properties of the samples. In Fig. 10, it is clear that the C/S and C/B samples have practically identical compressive rupture characteristics. Using a sintered BPY powder layer on vitreous silica as a substrate contributes to increase the maximal compressive stress of the samples despite having a wider distribution.

Considering these results, the vitreous silica substrate was chosen for the rest of the following experiments. Basalt substrates offer no major advantages and make the separation stage more complex, as the basalt is harder to cut. The 1 mm thick layer of sintered BPY brought interesting results but was considered hard to replicated and produce in large quantities in good conditions for the moment.

3.2. Mechanical behavior: effect of powder nature

On the other hand, leaving aside the substrate influence, the change in BPY analog powder type (Fig. 11, C/S, CA/S and A/S) significantly increased the mechanical resistance of the samples, with an average maximal compressive stress moving from 23 MPa for the samples made with 100 % crystalline powder to 46 MPa for samples made with 100 % amorphous powder.

Scanning electron microscope observations coupled with XRD experiments revealed that the phases present in C/S and CA/S samples, regardless of the additive manufacturing conditions, are mostly identical, as show in Fig. 12.

This can be linked to the rapid cooling kinetics of the melting pool, most of the volume being rearranged into a glass matrix, similar to the

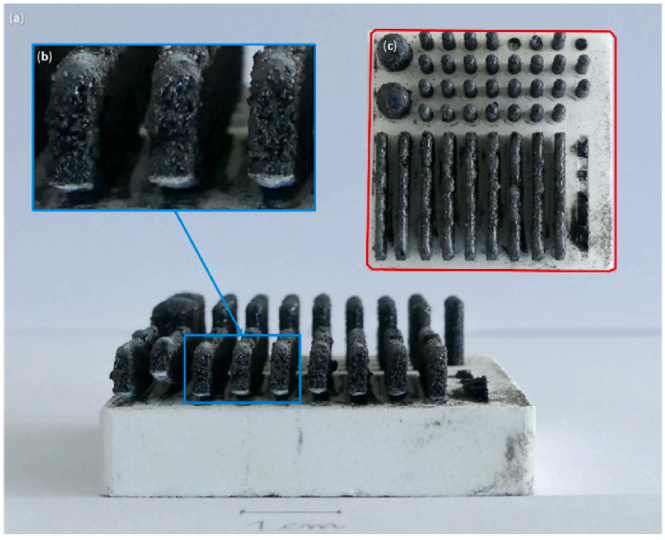

Fig. 9. Side view (a) of the C/S batch, with (b) a zoomed section showing an important lift of one edge of the parallelepipeds, with partially lifted substrate, and (c) top view.

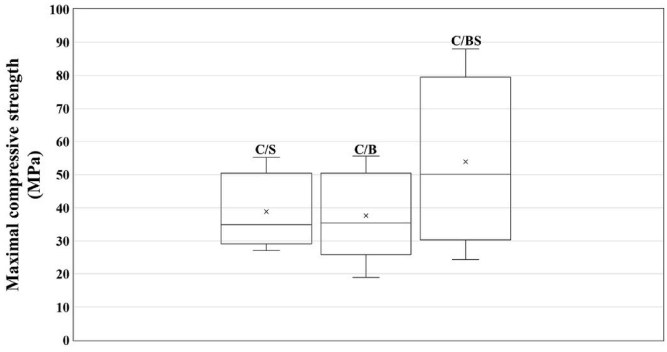

Fig. 10. From left to right: maximal compressive stress distributions of C/S, C/B, and C/BS on the basis of 6 samples per category. The cross indicates the mean value, the middle line the median, upper and lower bounds are the minimum and maximum values, and the two ends of the rectangle are the first and third quartiles.

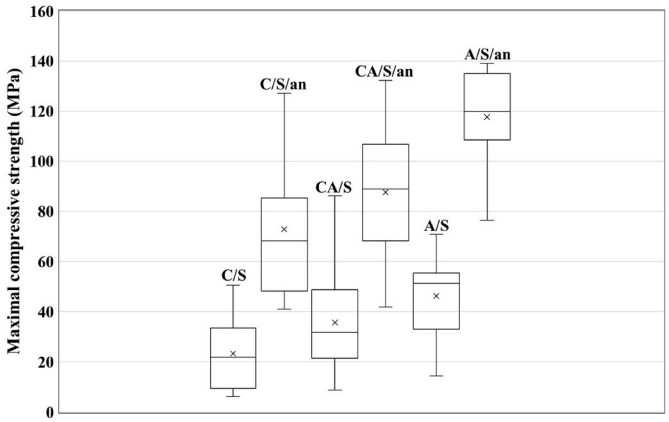

Fig. 11. Maximal compressive stress distributions based on 24 test results for (C/S) and (CA/S), and 12 test results for (C/S/an), (CA/S/an), (A/S) and (A/S/an) configurations. The cross indicates the mean value, the middle line the median, upper and lower bounds are the minimum and maximum values, and the two ends of the rectangle are the first and third quartiles.

amorphous powder prepared with controlled quench presented in section 2. In the volume of this amorphous matrix are still regularly found residual crystalline phases of various natures, both unmelted (kept the same particular shape as unprocessed BPY, Fig. 12c) and dendritic recrystallized ones (Fig. 12b). However, in the case of A/S grade, no crystalline peaks are detected despite the presence of dendritic crystals. It can therefore be concluded that the presence of recrystallized phases in the material is highly limited since they are undetectable with XRD. At the surface of these cylinders are predominantly found unaltered initial powder particles anchored in the amorphous phase resulting from laser melting, giving their coarse aspect to the samples. These observations are consistent with Vickers microhardness tests that showed an average hardness of 700Hv in the matrix, a typical value for a silicate-based glass [43]. Hydrostatic weighing and optical microscopy (Fig. 13) point out a prominent difference in aspect, number of cracks, and closed porosity ratio between C/S and CA/S samples, which can explain the difference in mechanical properties between these two configurations. Objects purely made from basaltic materials can be classified as ceramics, due to the iono-covalent nature of their atomic bonding, and thus are highly sensitive to the presence of defects as cracks and porosities in terms of mechanical properties. Such a decrease in porosity in the CA/S samples could be explained by the gain in mobility of the material, coming from the glass transition temperature characteristic to the amorphous phase, allowing pore mobility at the viscous state and, at higher temperature, complex mechanisms during viscous phase sintering [39]. Indeed, even if powder melting does occur at the sample scale, there are still certain kinetic aspects to consider: laser melting being extremely fast, it is conceivable that the material has time to melt and to solidify rapidly without the pores having time to be completely evacuated. The proportion of amorphous phase could therefore provide the extra mobility time needed to eliminate pores. These results suggest that exploiting areas of mature regolith (amorphous-rich) of the Moon could be quite beneficial as it would highly contribute in a natural manner to enhance the mechanical properties of the printed objects and structures.

Before considering the changes in maximum stress and Young's modulus values as a function of process parameters, it is interesting to consider the shape of the behavior curves in compression. The two types of curves observed during the study are illustrated in Fig. 14. For one curve, the rupture point is reached linearly, following a classical behavior of brittle ceramics. For the other curve, non-linearities (including jumps) are observed before reaching the maximum stress

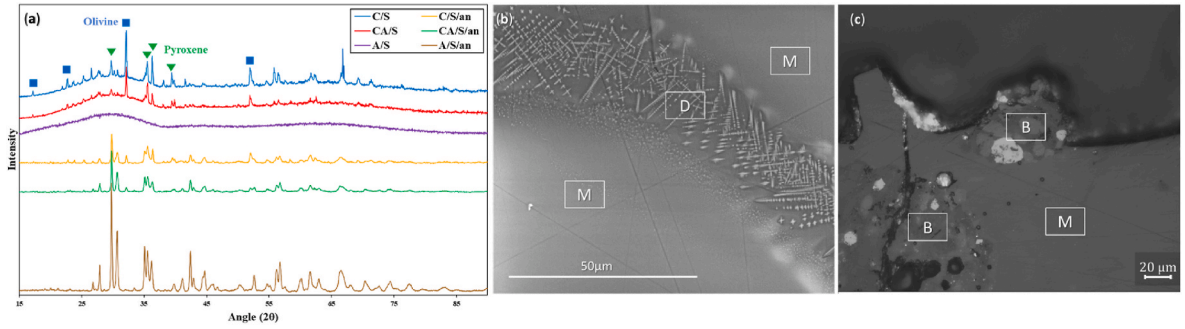

Fig. 12. (a) XRD diagrams of SLM manufactured samples, Two SEM images of a C/S cross section with a focus on **(b)** a post-fabrication crystallized dendritic formation (probably ilmenite or a similar phase) [D] in an amorphous matrix [M], and **(c)** on residual unmelted native basaltic particles [B].

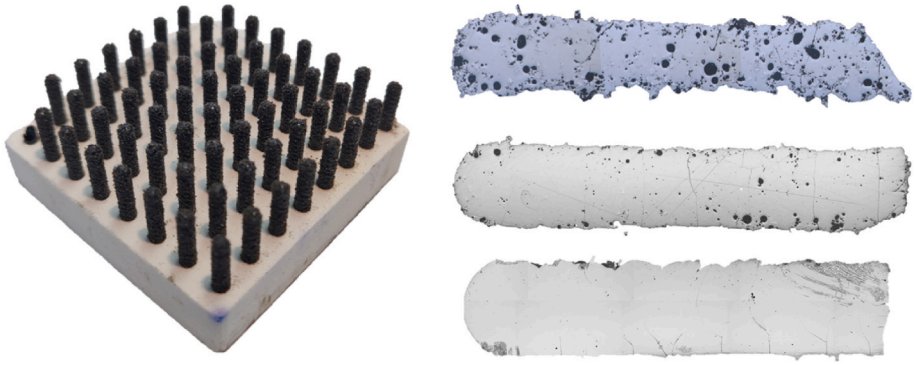

Fig. 13. (left) typical batch of 10 mm high and 3 mm diameter cylinders fabricated by SLM on their vitreous silica substrate and **(right)** cross sections in optical microscopy of such cylinders made with respectively 100 % native crystalline BPY powder (top, C/S configuration), with a mix of 50 wt% native crystalline BPY/50 wt% amorphous BPY (middle, CA/S configuration), 100 % amorphous BPY powder (bottom, A/S configuration).

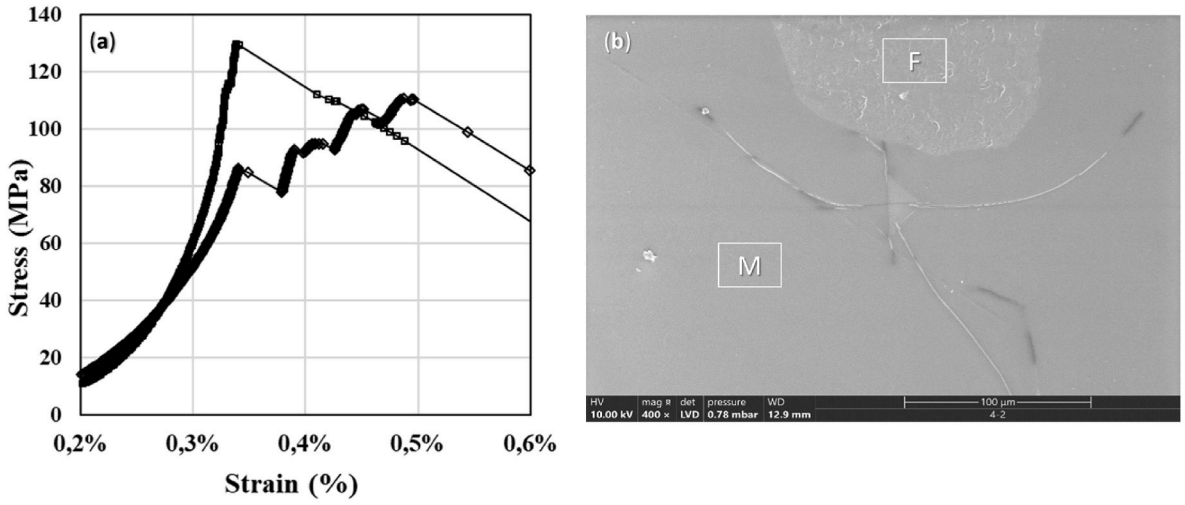

Fig. 14. **(a)** Typical compression behavior curves for two CA/S samples and **(b)** Vickers microhardness indent. Illustration of the presence ok cracks at the indent corners, of crack propagation in the amorphous matrix, of crack deviation and of crack stop by an unmelted forsterite particle [F].

value. This second behavior seems to demonstrate a capacity of the material to resist the initiation and sudden and catastrophic propagation of cracks. It was also observed during the tests (both visually and acoustically) that the 3D-printed objects can be damaged without completely collapsing, contrasting with their ceramic nature. This behavior can probably be linked to the crack deviation mechanisms observed after Vickers indentation tests, caused by the presence of crystalline phases (i.e. unmelted phases and phases that crystallized during cooling after laser melting).

3.3. *Mechanical behavior: annealing effect*

After SLM fabrication, samples are mostly made of a metastable amorphous matrix, which is probably not an optimal case for mechanical properties: indeed, glass components generally have weaker hardness and stress resistance than their crystalline counterpart and can accumulate residual stresses. To assess those statements, a quarter of the samples from C/S, CA/S and A/S batches were then randomly selected and annealed following instructions from section 2.2 (C/S/an, CA/S/an and A/S/an). After conclusive XRD analysis confirming the predominant diopsidic nature of the annealed samples (Fig. 12), Vickers microhardness and compressive test results (Fig. 11) showed a significant enhancement of mechanical properties, with a new microhardness of 900Hv of the matrix and a more than doubled average maximum stress moving from untreated to annealed samples categories.

The evolution of both Young's modulus and of maximum stress value as a function of the closed porosity can be considered (Fig. 15). Results show that the annealing process leads to a significant decrease of the samples' closed porosity, and to an increase of the two considered mechanical properties. This tendency to improve properties as porosity decreases is standard for ceramics [44], and in the case of high Young's modulus samples, the highest obtained values are close to what one could find for bulk natural basalt (around 80 GPa [45]). A quite linear relation between samples' stiffness and maximal compressive stress could be observed. It can be explained by the fact that rupture in elastic materials like ceramics is strain dependent. Results show here a rupture

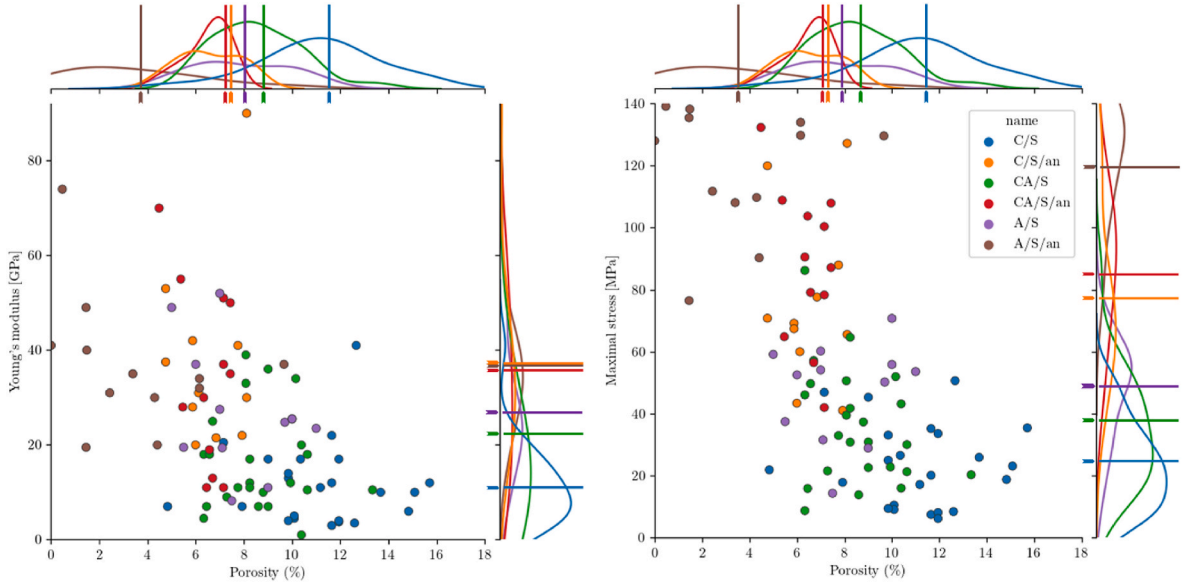

Fig. 15. Correlation between **(left)** samples Young's modulus and porosity, **(right)** maximal compressive stress and porosity. Kernel densities of those considered parameters are represented on the sides and top of the scattered plot as well as markers that indicate the average value, to highlight the translation between the different groups' values dispersion.

strain value close to 0.2 % strain for most of the tested cylinders.

Even if the correlation between the considered mechanical properties and porosity is clear, explanations on why the different categories (annealed samples and their counterparts) do not have the same porosity need to be identified. Various mechanisms can still be considered. The viscous state of the amorphous material, reached during the annealing process between the glass transition temperature and the cold crystallization area, could be enough to start viscous flow mechanisms and seal pre-existing voids like small porosities and microcracks. Furthermore, the diopsidic augite could also be a denser material than glass, leading to a shrinkage of the samples and therefore to a diminution of porosity.

SEM observations of compression fractured samples underline the changes in material structure and properties identified earlier (Fig. 16). While C/S and CA/S (respectively rows a and c in Compression fracture surfaces on (a) a C/S sample, (b) a C/S/an sample, (c), a CA/S sample and (d), a CA/S/an sample (SEM images)) exhibit smooth surfaces even at high magnifications, except for some regular crack plane deflections typical of glass materials, C/S/an and CA/S/an (respectively rows b and d) show much greater topographical irregularities, similar to polycrystalline brittle materials with transgranular fractures. Moreover, two types of fracture surfaces are presented and visible in Fig. 17, for annealed samples (C/S/an and CA/S/an). On the one hand, transgranular rupture surfaces due to the compressive solicitation are clearly seen. On the other hand, the green highlighted areas of (b4-b5) and (d4-d5) images are surfaces on which the three-dimensional shape of crystals or grains is recognizable. They can be considered as being the result of surface crystallization phenomena that have occurred during the annealing process on pre-existing microcracks, probably formed during the SLM step. Those observations are additional proof that: 1) the annealing treatment affects all the sample volume, including its core and −2) the SLM and/or substrate separation step can induce rupture microcracking in samples.

3.4. *Reproducibility and comparison to literature*

Despite exhibiting interesting trends in terms of mechanical properties when varying process configurations (substrate and powder nature, annealing treatment), every configuration shows a wide range of properties distribution, in terms of porosity, Young's modulus, and more particularly maximal compressive stress. However, the compressive stress distribution for annealing thermal treated categories shows practically no overlay with its non-annealed counterpart, weakest annealed samples being as mechanically resistant as the best samples in other categories. Moreover, comparing compressive stress distributions

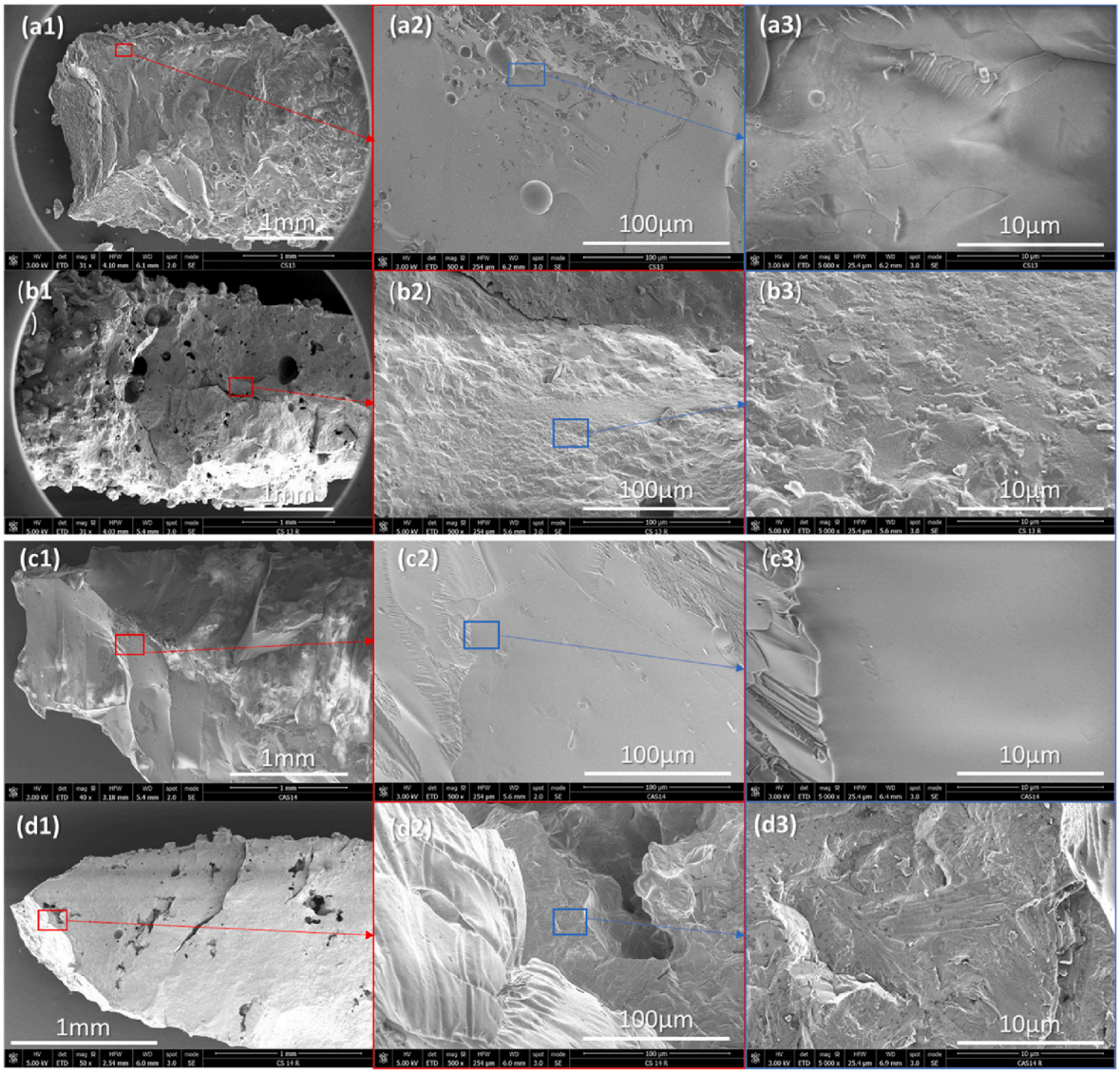

Fig. 16. Compression fracture surfaces on (a) a C/S sample, (b) a C/S/an sample, (c), a CA/S sample and (d), a CA/S/an sample (SEM images).

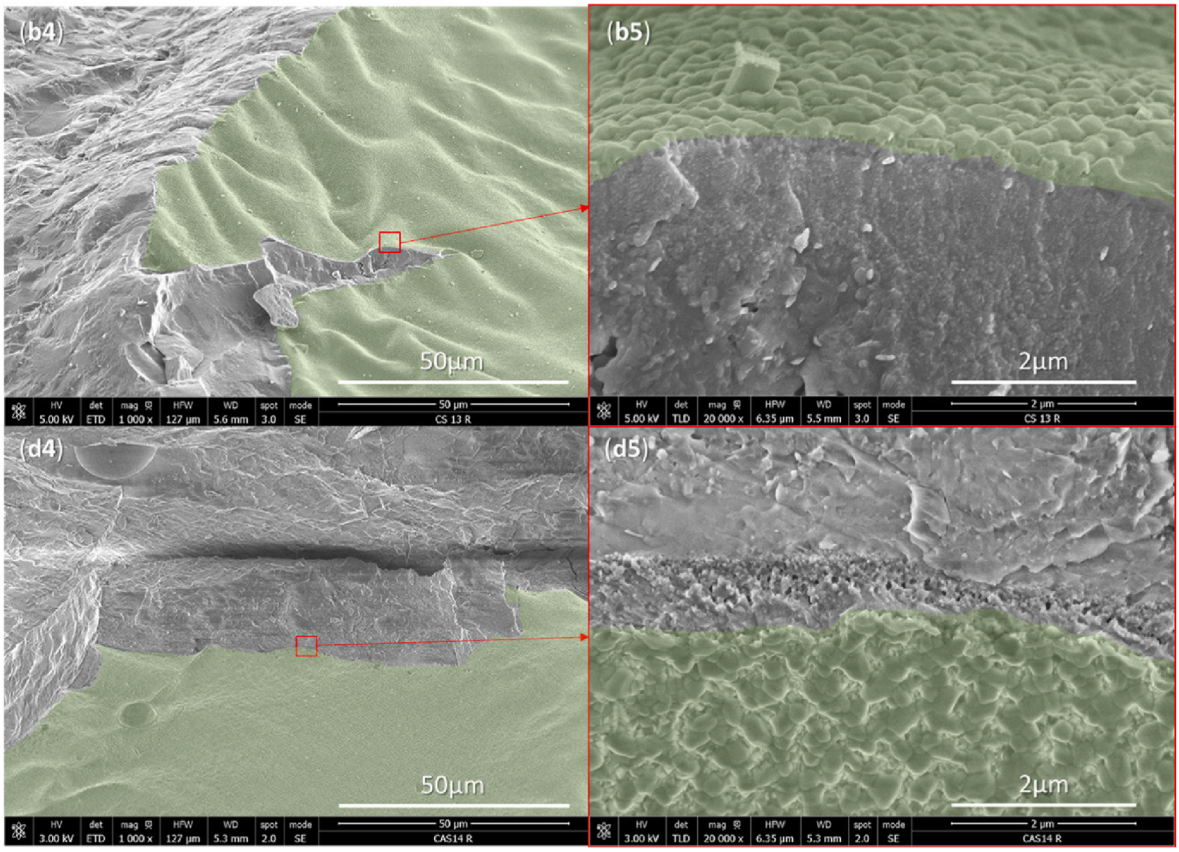

Fig. 17. SEM pictures of C/S/an (b) and CA/S/an (d) samples after compressive tests. Pre-existing and exposed surfaces during annealing are highlighted in green, while the other areas are fracture surfaces formed during mechanical tests. (For interpretation of the references to colour in this figure legend, the reader is referred to the Web version of this article.)

of samples with strictly identical manufacturing parameters but from different SLM batches, also display different property ranges. This can be precisely seen by comparing C/S compression tests results in Fig. 10 with Fig. 11, which are at identical experimental parameters. In the future, it appears essential to identify factors creating the most variability and to limit their effect, whether the dispersion of results is within a batch or between different ones. As an example, the substrate separation step could be the source of additional mechanical stresses, which can significantly vary from one batch to another and highly impact sample performances. Limiting such an impact could be done by introducing an easily breakable micropillars network between the sample and the substrate during additive manufacturing. That way, every variability due to the substrate would be negligible. The successive recycling of powder between every experiment could also explain

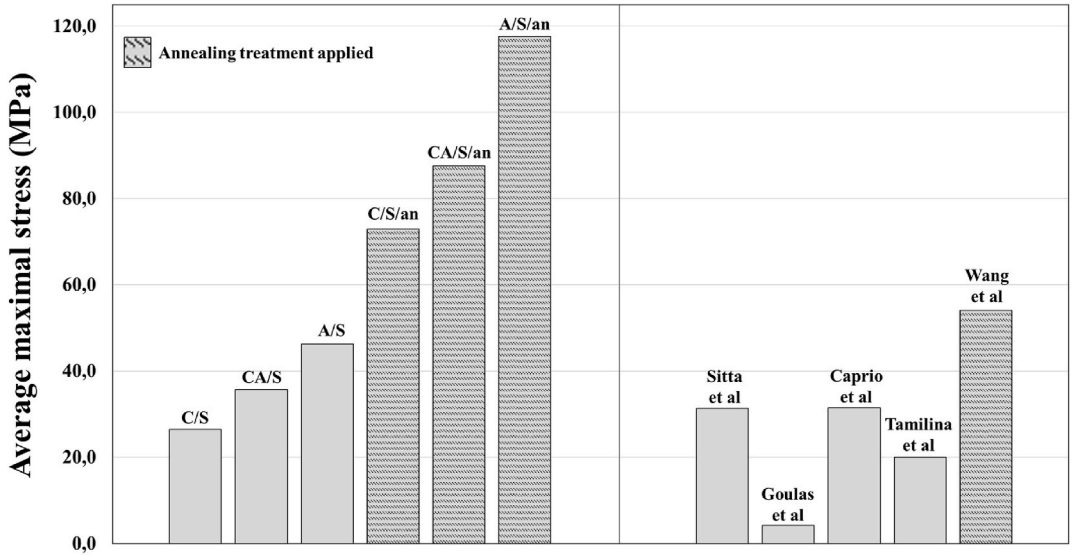

Fig. 18. (Left) Summary of average maximal compressive strengths of presented configurations on silica substrates (from C/S to A/S/an) compared to **(Right)** several SLM results on simulants referenced in the literature [16–18,47,48].

the difference in mechanical properties. It could also be considered to reduce the wrapping effect, which is highly variable from one sample to another, by lowering the powder layer thickness and laser power or increasing laser scanning speed at the same time. This would lower surface energy distribution, and so diminish melting pool temperature and thermal gradient in the same way, and still preserve the same volumetric energy density, as suggested in previous papers [42,46]. Compared to other studies based on laser powder bed fusion of regolith simulants (Fig. 18), the average compressive maximum strength of the presented BPY-based cylinders is at a comparable strength level. For the configurations considered in this study, the results obtained after annealing show the ability to achieve higher compressive rupture stress levels than those obtained previously. It is still important to note a few major differences [47]: used cubic samples made with highland simulant as well as [17], and the value selected from Ref. [48] is the best case scenario, with an annealing treatment as well as a compressive test in the parallel direction of the additive manufacturing layers.

4. Conclusion and prospects

In this paper we characterized a new lunar mare analog named BPY for Basalt of Pic d'Ysson. Its grain size distribution, chemical and mineral compositions, as well as its main thermal transformations have been documented as a base for selective laser melting experiments. A simplified experimental design, based on the variation of three major parameters, namely the nature of the powder, the nature of the substrate and the application or non-application of an annealing post-treatment, have been implemented. Uniaxial compressive tests showed a strong effect of the substrate interphase physical properties but not of its chemical nature, for the considered substrate type; **the relevance of the presence of amorphous powder in the analog powder is also demonstrated with a clear improvement of sample porosity and mechanical properties**, underlying the importance of the selection of a mature regolith area as a source for ISRU manufacturing. **After annealing, promising values of compression rupture stress have been reached, close to what one could obtain with sintered samples** [49]. The annealing process contributes by changing the nature of the material from a glassy state to a polycrystalline one and by reducing residual stresses generated during the SLM process. A more comprehensive investigation of the optical and thermal properties of the BPY at high temperatures as emissivity and granular thermal conductivity is ongoing, with the objective of modeling precisely the heating, melting, and solidification processes, and predicting the best parameters for rupture strengths and Young's modulus. In particular, computer modeling could be a way to identify a lasing strategy to create an in-situ annealing effect during the additive manufacturing step and avoid a post-treatment step which is not ideal in a lunar outpost concept, as it partially cancels one of the two main advantages of direct additive manufacturing. The feasibility of this in-situ annealing will depend on the kinetic of crystallization of the BPY analog. In parallel, we will explore the effect of tuning BPY chemical composition with oxide addition to assess the implications when one considers the regolith deriving from the diversity of the lunar mare basalts. Taken together, these elements should provide a general roadmap for generating regolith objects with controlled precision and improved mechanical strength.

CRediT authorship contribution statement

Julien Granier: Writing – original draft, Visualization, Investigation, Formal analysis, Data curation, Conceptualization. **Thierry Cutard:** Writing – review & editing, Validation, Supervision, Resources, Project administration, Methodology, Investigation, Funding acquisition, Formal analysis, Data curation, Conceptualization. **Patrick Pinet:** Writing – review & editing, Supervision, Resources, Investigation, Conceptualization. **Yannick Le Maoult:** Writing – review & editing, Supervision, Resources, Investigation, Conceptualization. **Serge Chevrel:** Writing – review & editing, Supervision, Resources, Investigation, Conceptualization. **Thierry Sentenac:** Writing – review & editing, Supervision, Resources, Investigation, Conceptualization. **Jean-Jacques Favier:** Funding acquisition, Conceptualization.

Declaration of competing interest

The authors declare that they have no known competing financial interests or personal relationships that could have appeared to influence the work reported in this paper.

Acknowledgments

Gratitude toward doctoral school Ecole Doctorale Aéronautique Astronautique (ED 427) for funding this PhD thesis work. Many thanks to Patrick Houizot and Tanguy Rouxel from the Institut de Physique de Rennes (France) who melted and quenched BPY, providing us with the amorphous material, and Franck Collas from Mettler Toledo for the development of the DSC analysis at high temperature. Appreciation to Centre d'Etudes et d'expertise sur les Risques, la Mobilité et l'Aménagement (Cerema, Toulouse, France), Géosciences Environnement Toulouse laboratory (France), which helped us preparing and characterizing our analog. Special thanks to the ICA technical staff members (Adrien Lieurey for additive manufacturing and powder preparation, Karim Choquet for XRD analysis, Karine Vieillevigne for SEM analysis) and interns (Mélissa Marchi, Vincent Gabriot, Lou Narbonne, Thomas Cabos) involved in this project which is one of the research priorities of the ISRU Toulouse Task Force. J.G., P.P. and S.C. have benefited from the support of the French Space Agency (CNES) in a project in conjunction with the Chang'e-4 mission/VNIS instrument. The authors also acknowledge the support provided by the reviewers and thank them for their feedback, which greatly improved the quality and clarity of the article.

References

[1] S. Creech, J. Guidi, D. Elburn, Artemis: an overview of NASA's activities to return humans to the Moon, in: 2022 IEEE AEROSPACE CONFERENCE (AERO), IEEE, New York, 2022, https://doi.org/10.1109/AERO53065.2022.9843277.

[2] Y. Lin, W. Yang, H. Zhang, H. Hui, S. Hu, L. Xiao, J. Liu, Z. Xiao, Z. Yue, J. Zhang, Y. Liu, J. Yang, H. Lin, A. Zhang, D. Guo, S. Gou, L. Xu, Y. He, X. Zhang, L. Qin, Z. Ling, X. Li, A. Du, H. He, P. Zhang, J. Cao, X. Li, Return to the Moon: new perspectives on lunar exploration, Sci. Bull. 69 (2024) 2136–2148, https://doi.org/10.1016/j.scib.2024.04.051.

[3] T. Victor Joseph, India's space exploration roadmap, in: 67th Session of UNCOPUOS, Vienna International Centre, 2024. https://www.unoosa.org/documents/pdf/copuos/2024/Technical_Presentations/26Day/6_item_15_Updated_India_Space_Exploration_Roadmap_21_June_2024-edited_1.pdf. (Accessed 23 July 2024).

[4] Y. Ishihara, T. Shimomura, R. Nishitani, M. Aida, Mizuno, JAXA's mission instruments in the ISRO-JAXA joint lunar polar exploration (LUPEX) project -overview and developing status, in: 55th Lunar and Planetary Science Conference, 2024. https://www.hou.usra.edu/meetings/lpsc2024/pdf/1761.pdf.

[5] S.D. Mey, Terrae Novae 2030+ Strategy Roadmap, (n.d.). https://esamultimedia.esa.int/docs/HRE/Terrae_Novae_2030+strategy_roadmap.pdf.

[6] Y. Akisheva, Y. Gourinat, Utilisation of Moon regolith for radiation protection and thermal insulation in permanent lunar habitats, Appl. Sci. 11 (2021) 3853, https://doi.org/10.3390/app11093853.

[7] P. Zhang, W. Dai, R. Niu, G. Zhang, G. Liu, X. Liu, Z. Bo, Z. Wang, H. Zheng, C. Liu, H. Yang, Y. Bai, Y. Zhang, D. Yan, K. Zhou, M. Gao, Overview of the lunar in situ resource utilization techniques for future lunar missions, Space: Sci. Technol. 3 (2023), https://doi.org/10.34133/space.0037.

[8] M. Isachenkov, I. Gorokh, E. Makarov, D. Verkhoturov, P. Khmelenko, N. Garzaniti, A. Golkar, Technical evaluation of additive manufacturing technologies for in-situ fabrication with lunar regolith, Adv. Space Res. 71 (2023) 2656–2668, https://doi.org/10.1016/j.asr.2022.07.075.

[9] S.L. Taylor, A.E. Jakus, K.D. Koube, A.J. Ibeh, N.R. Geisendorfer, R.N. Shah, D. C. Dunand, Sintering of micro-trusses created by extrusion-3D-printing of lunar regolith inks, Acta Astronaut. 143 (2018) 1–8, https://doi.org/10.1016/j.actaastro.2017.11.005.

[10] N. Leach, A. Carlson, B. Khoshnevis, M. Thangavelu, Robotic construction by contour crafting: the case of lunar construction, Int. J. Architect. Comput. 10 (2012) 423–438, https://doi.org/10.1260/1478-0771.10.3.423.

[11] M. Liu, W. Tang, W. Duan, S. Li, R. Dou, G. Wang, B. Liu, L. Wang, Digital light processing of lunar regolith structures with high mechanical properties, Ceram. Int. 45 (2019) 5829–5836, https://doi.org/10.1016/j.ceramint.2018.12.049.

[12] G. Cesaretti, E. Dini, X. De Kestelier, V. Colla, L. Pambaguian, Building components for an outpost on the Lunar soil by means of a novel 3D printing technology, Acta Astronaut. 93 (2014) 430–450, https://doi.org/10.1016/j.actaastro.2013.07.034.

[13] S. Lim, S. Reeve, E. Lekuona, A. Garbayo, T. Le Toux, A. Morse, J. Bowen, M. Anand, Challenges in the microwave heating of lunar regolith – analysis through the design of a microwave heating Demonstrator (MHD) payload, Adv. Space Res. 69 (2022) 751–760, https://doi.org/10.1016/j.asr.2021.10.038.

[14] M. Fateri, A. Gebhardt, Process parameters development of selective laser melting of lunar regolith for on-site manufacturing applications, Int. J. Appl. Ceram. Technol. 12 (2015) 46–52, https://doi.org/10.1111/ijac.12326.

[15] A. Zocca, J. Wilbig, A. Waske, J. Günster, M.P. Widjaja, C. Neumann, M. Clozel, A. Meyer, J. Ding, Z. Zhou, X. Tian, Challenges in the technology development for additive manufacturing in space, Chin. J. Mech. Eng.: Additive Manufacturing Frontiers 1 (2022) 100018, https://doi.org/10.1016/j.cjmeam.2022.100018.

[16] K. Farries, P. Visintin, S. Smith, Direct laser sintering for lunar dust control: an experimental study of the effect of simulant mineralogy and process parameters on product strength and scalability. https://doi.org/10.1016/j.conbuildmat.2022.129191, 2022.

[17] L. Caprio, A.G. Demir, B. Previtali, B.M. Colosimo, Determining the feasible conditions for processing lunar regolith simulant via laser powder bed fusion, Addit. Manuf. 32 (2020) 101029, https://doi.org/10.1016/j.addma.2019.101029.

[18] A. Goulas, J.G. Binner, D.S. Engstrøm, R.A. Harris, R.J. Friel, Mechanical behaviour of additively manufactured lunar regolith simulant components, Proc. Inst. Mech. Eng., Part L 233 (2019) 1629–1644, https://doi.org/10.1177/1464420718777932.

[19] L.A. Taylor, C.M. Pieters, D. Britt, Evaluations of lunar regolith simulants, Planet. Space Sci. 126 (2016) 1–7, https://doi.org/10.1016/j.pss.2016.04.005.

[20] A.L. Souchon, P.C. Pinet, S.D. Chevrel, Y.H. Daydou, D. Baratoux, K. Kurita, M. K. Shepard, P. Helfenstein, An experimental study of Hapke's modeling of natural granular surface samples, Icarus 215 (2011) 313–331, https://doi.org/10.1016/j.icarus.2011.06.023.

[21] A.M. Cord, P.C. Pinet, Y. Daydou, S.D. Chevrel, Planetary regolith surface analogs:: optimized determination of Hapke parameters using multi-angular spectro-imaging laboratory data, Icarus 165 (2003) 414–427, https://doi.org/10.1016/S0019-1035(03)00204-5.

[22] N. Sakatani, K. Ogawa, M. Arakawa, S. Tanaka, Thermal conductivity of lunar regolith simulant JSC-1A under vacuum, Icarus 309 (2018) 13–24, https://doi.org/10.1016/j.icarus.2018.02.027.

[23] N. Sakatani, K. Ogawa, Y. Iijima, M. Arakawa, S. Tanaka, Compressional stress effect on thermal conductivity of powdered materials: measurements and their implication to lunar regolith, Icarus 267 (2016) 1–11, https://doi.org/10.1016/j.icarus.2015.12.012.

[24] A. Zocca, M. Fateri, D. Al-Sabbagh, J. Günster, Investigation of the sintering and melting of JSC-2A lunar regolith simulant, Ceram. Int. 46 (2020) 14097–14104, https://doi.org/10.1016/j.ceramint.2020.02.212.

[25] M. Fateri, R. Sottong, M. Kolbe, J. Gamer, M. Sperl, A. Cowley, Thermal properties of processed lunar regolith simulant, Int. J. Appl. Ceram. Technol. 16 (2019) 2419–2428, https://doi.org/10.1111/ijac.13267.

[26] D. Ignjatović Stupar, G. Robert Chabrol, A.R. Ibrahim Baraze, S. Lecler, A. Tessier, T. Cutard, J. Brendle, Feasibility of additive manufacturing processes for lunar soil simulants, Adv.Tech&Mat. 47 (2022) 39–43, https://doi.org/10.24867/ATM-2022-1-007.

[27] B. Reitz, C. Lotz, N. Gerdes, S. Linke, E. Olsen, K. Pflieger, S. Sohrt, M. Ernst, P. Taschner, J. Neumann, E. Stoll, L. Overmeyer, Additive manufacturing under lunar gravity and microgravity, Microgravity Sci. Technol. 33 (2021) 25, https://doi.org/10.1007/s12217-021-09878-4.

[28] S. Linke, L. Windisch, N. Kueter, J.E. Wanvik, A. Voss, E. Stoll, C. Schilde, A. Kwade, TUBS-M and TUBS-T based modular Regolith Simulant System for the support of lunar ISRU activities, Planet. Space Sci. 180 (2020) 104747, https://doi.org/10.1016/j.pss.2019.104747.

[29] B.L. Jolliff, M.A. Wieczorek, C.K. Shearer, C.R. Neal, New Views of the Moon, Walter de Gruyter GmbH & Co KG, 2018.

[30] C.S. Ray, S.T. Reis, S. Sen, J.S. O'Dell, JSC-1A lunar soil simulant: characterization, glass formation, and selected glass properties, J. Non-Cryst. Solids 356 (2010) 2369–2374, https://doi.org/10.1016/j.jnoncrysol.2010.04.049.

[31] W.D. Carrier III, G.R. Olhoeft, W. Mendell, Physical Properties of the Lunar Surface (1991). https://ui.adsabs.harvard.edu/abs/1991lsug.book..475C. (Accessed 24 January 2022).

[32] J. Carignan, P. Hild, G. Mevelle, J. Morel, D. Yeghicheyan, Routine analyses of trace elements in geological samples using flow injection and low pressure on-line liquid chromatography coupled to ICP-MS: a study of geochemical reference materials BR, DR-N, UB-N, AN-G and GH, Geostand. Geoanal. Res. 25 (2001) 187–198, https://doi.org/10.1111/j.1751-908X.2001.tb00595.x.

[33] T.A. Giguere, G.J. Taylor, B.R. Hawke, P.G. Lucey, The titanium contents of lunar mare basalts, Meteorit & Planetary, Science 35 (2000) 193–200, https://doi.org/10.1111/j.1945-5100.2000.tb01985.x.

[34] E. Hill, M.J. Mellin, B. Deane, Y. Liu, L.A. Taylor, Apollo sample 70051 and high- and low-Ti lunar soil simulants MLS-1A and JSC-1A: implications for future lunar exploration, J. Geophys. Res.: Planets 112 (2007), https://doi.org/10.1029/2006JE002767.

[35] J.M. Long-Fox, Z.A. Landsman, P.B. Easter, C.A. Millwater, D.T. Britt, Geomechanical properties of lunar regolith simulants LHS-1 and LMS-1, Adv. Space Res. (2023), https://doi.org/10.1016/j.asr.2023.02.034.

[36] V.S. Engelschiøn, S.R. Eriksson, A. Cowley, M. Fateri, A. Meurisse, U. Kueppers, M. Sperl, EAC-1A: a novel large-volume lunar regolith simulant, Sci. Rep. 10 (2020) 5473, https://doi.org/10.1038/s41598-020-62312-4.

[37] H. Kanamori, S. Udagawa, T. Yoshida, S. Matsumoto, K. Takagi, Properties of lunar soil simulant manufactured in Japan, in: Space 98, American Society of Civil Engineers, Albuquerque, New Mexico, United States, 1998, pp. 462–468, https://doi.org/10.1061/40339(206)53.

[38] Y. Zheng, S. Wang, Z. Ouyang, Y. Zou, J. Liu, C. Li, X. Li, J. Feng, CAS-1 lunar soil simulant, Adv. Space Res. 43 (2009) 448–454, https://doi.org/10.1016/j.asr.2008.07.006.

[39] K.W. Farries, P. Visintin, S.T. Smith, P. van Eyk, Sintered or melted regolith for lunar construction: state-of-the-art review and future research directions, Construct. Build. Mater. 296 (2021) 123627, https://doi.org/10.1016/j.conbuildmat.2021.123627.

[40] S. Yilmaz, O.T. Özkan, V. Günay, Crystallization kinetics of basalt glass, Ceram. Int. 22 (1996) 477–481, https://doi.org/10.1016/0272-8842(95)00118-2.

[41] A. Goulas, R.J. Friel, 3D printing with moondust. https://doi.org/10.1108/RPJ-02-2015-0022, 2016.

[42] T. Shen, W. Yao, X. Quan, In-situ visualization of powder wrapping behavior in millimeter-scale-beam lunar regolith powder bed fusion, Powder Technol. 425 (2023) 118552, https://doi.org/10.1016/j.powtec.2023.118552.

[43] T. Rouxel, J. Jang, U. Ramamurty, Indentation of glasses, Prog. Mater. Sci. 121 (2021) 100834, https://doi.org/10.1016/j.pmatsci.2021.100834.

[44] S. Meille, M. Lombardi, J. Chevalier, L. Montanaro, Mechanical properties of porous ceramics in compression: on the transition between elastic, brittle, and cellular behavior, J. Eur. Ceram. Soc. 32 (2012) 3959–3967, https://doi.org/10.1016/j.jeurceramsoc.2012.05.006.

[45] R.A. Schultz, Limits on strength and deformation properties of jointed basaltic rock masses, Rock Mech. Rock Eng. 28 (1995) 1–15, https://doi.org/10.1007/BF01024770.

[46] D. Kaya, M. Abdelmoula, G. Küçüktürk, D. Grossin, A. Stamboulis, A novel approach for powder bed fusion of ceramics using two laser systems, Materials 16 (2023) 2507, https://doi.org/10.3390/ma16062507.

[47] L.A. Sitta, M. Lavagna, 3D printing of moon highlands regolith simulant, Th International Astronautical Congress (2018).

[48] R. Wang, G. Qiao, G. Song, Additive manufacturing by laser powder bed fusion and thermal post-treatment of the lunar-regolith-based glass-ceramics for in-situ resource utilization, Construct. Build. Mater. 392 (2023) 132051, https://doi.org/10.1016/j.conbuildmat.2023.132051.

[49] S.J. Indyk, H. Benaroya, A structural assessment of unrefined sintered lunar regolith simulant, Acta Astronaut. 140 (2017) 517–536, https://doi.org/10.1016/j.actaastro.2017.09.018.